(Received 13 April 2025, Accepted 26 May 2025, Scheduled 6 June 2025)

Simplified Duty Cycle Modulation Model Predictive Current Control of PMSM without Cost Function

Dingdou Wen[1], Chaoyi Liu[1], Yanqin Zhang[1], and Zhun Cheng[2,*]

[1]Hunan University of Technology, Zhuzhou 412007, China
[2]Hunan Railway Professional Technology College, Zhuzhou 412001, China

ABSTRACT: To reduce the prediction times and algorithm complexity of model predictive current control (MPCC) for permanent magnet synchronous motor (PMSM), a simplified duty cycle modulation model predictive current control without cost function (SDCM-MPCC) method is proposed. The proposed method uses two fixed voltage vectors to generate the three-phase duty cycles for any sector, which is directly applied to the inverter after correction, without using a cost function to traverse the combination and modulation of voltage vectors in different sectors with only 1 prediction. Deadbeat control on the *d*-*q* axis current is performed simultaneously to obtain the duty cycle for two fixed voltage vectors. The output voltage vectors can cover any amplitude and direction, effectively reducing current ripple and phase current harmonics. Simulations and experiments confirm the method's effectiveness and feasibility.

1. INTRODUCTION

With the global energy structure shifting towards low-carbon, permanent magnet synchronous motor (PMSM) has been widely used in fields, such as electric vehicles, new energy generation, and aerospace due to its advantages of high power density, high efficiency, and wide speed range [1–4]. Model predictive current control (MPCC) has strong nonlinear constraints and multi-objective control capabilities, and its structure is simple and easy to implement. It has also been widely used in power electronics and electrical transmission [5, 6].

The classical finite control set model predictive control traverses all basic voltage vectors of the inverter in each cycle, and the cost function value corresponding to each vector is obtained through 7 calculations per cycle, and the one with the smallest cost function value is selected to act on the inverter [7]. However, due to the application of only a single vector throughout the entire cycle and a fixed duty cycle of 1, the current and torque ripple are relatively large in steady state. Consequently, some scholars have proposed a multi-vector control method, which uses two or three voltage vectors to act on the inverter in each cycle [8–10]. In [8], two voltage vectors are selected to act on the inverter in each cycle, effectively reduce current ripple. In [9], the expected voltage vector is synthesized by three voltage vectors in each cycle, which can cover any direction and amplitude and more accurately track the reference current. In [10], virtual vectors are introduced, and a hierarchical multi-level optimization control algorithm is used to obtain the main control set and the extended control set, solving the problem of limited modulation range in traditional methods. However, bus voltage fluctuations or dead zone effects may cause synthesis errors. In [8–10], the steady-state performance is improved by increasing the number of vectors. However, as the number of vectors increases, especially when being faced with issues such as selecting vector combinations, optimizing cost functions, and calculating duty cycles, the computational workload also becomes much heavier. To simplify the vector selection process, in [11], the first voltage vector is determined through cost function traversal optimization, and the second vector is only selected from three candidate vectors. In [12], only three non-adjacent voltage vectors are traversed, and two of them are determined by the cost function value relationship, reducing the computational complexity to three times. Although [11, 12] reduce iterations compared to [8–10], the global optimal combination may be overlooked.

The core basis for selecting the optimal vector is the cost function, and a reasonable design of the cost function can improve the accuracy of current control [13]. However, traditional cost functions rely solely on prediction errors, and control inputs may not be smooth. In [14], the current error at the switching point is introduced into the cost function, reducing the current ripple caused by the switching action. Refs. [15, 16] proposed dual cost functions. Specifically, in [15], different cost functions are used for steady state and transient states, with a decrease in switching frequency during steady state and a rapid response during transient state. In [16], the first cost function (J_1) is used to balance current error and switching frequency, while the second cost function (J_2) aims to suppress harmonics. However, improper design of the dual cost function switching mechanism may lead to system stability issues, and the defect of high computational complexity in traversal optimization still exists. To further simplify the computational complexity of MPCC, some scholars have proposed abandoning the cost function and solving the optimal solution with only one computation. In [17], the first voltage vector is directly determined by

* Corresponding author: Zhun Cheng (120277982@qq.com).

the region where the reference voltage vector is located, and the second voltage vector is obtained using the mathematical auxiliary line method without the need for traversal and optimization. However, precise calculation of the reference voltage vector, determination of sectors, and selection of auxiliary lines are required for the controller. In [18], a voltage vector selection table based on current tracking error is designed, which eliminates the process of cost function optimization and reconstructs the three-phase duty cycle, reducing computational complexity. However, duty cycle reconstruction may lead to frequent changes in switch signals.

Once the optimal voltage vector has been identified, how to accurately calculate the duty cycle has a critical impact on the control effect [19]. The traditional duty cycle calculation method requires first calculating the current slope, but the calculation of the current slope depends on real-time measurements of current and voltage, and measurement errors can affect the accuracy of the duty cycle. To optimize the duty cycle, [20] proposed that only a simple constant and the ratio of current tracking error are needed to calculate the duty cycle, reducing computational complexity and parameter sensitivity. However, current sampling noise may cause duty cycle jitter. In [21], the duty cycle is calculated by the ratio of the reference speed to the rated speed, which is simple to calculate. However, changes in speed or load may lead to a decrease in control performance. In [22], the duty cycle of each candidate vector is inversely proportional to its cost function value, which not only reduces algorithm complexity but also enhances parameter robustness. However, the inverse duty cycle allocation depends on the quality of vector selection. If the globally optimal vector is missed, the duty cycle cannot be allocated to the optimal one.

To address the issues mentioned above, reduce the algorithm complexity and prediction times, while maintaining good steady-state performance, a simplified duty cycle modulation model predictive current control without cost function method is proposed. Firstly, two fixed phase voltage vectors are selected to generate the three-phase duty cycle of any sector without cost function. Secondly, the duty cycle of the two fixed voltage vectors is obtained using the deadbeat control principle, and the three-phase duty cycle is calculated from it to directly drive the PMSM. Finally, simulations and experiments demonstrate that the proposed method has low complexity, effectively reduces d-q axis current ripple and phase current harmonics, and exhibits superior steady-state performance.

The contributions of this study are detailed below:

(i) The proposed method can generate three-phase duty cycles for any sector using two fixed voltage vectors, without cost function traversal optimization, and only requires one prediction.

(ii) To address the issue of high complexity in traditional current slope calculation, an innovative duty cycle calculation is proposed, which can quickly determine the three-phase duty cycle and directly drive PMSM without the need for driving signal generation and modulation.

(iii) The amplitude and direction of the output voltage vector can be adjusted arbitrarily, significantly suppressing current ripple and phase current harmonics.

2. TWO-LEVEL INVERTER TOPOLOGY AND PMSM MATHEMATICAL MODEL

2.1. Two-Level Inverter Topology

This article focuses on a two-level inverter, and the power topology used to drive PMSM is presented in Fig. 1.

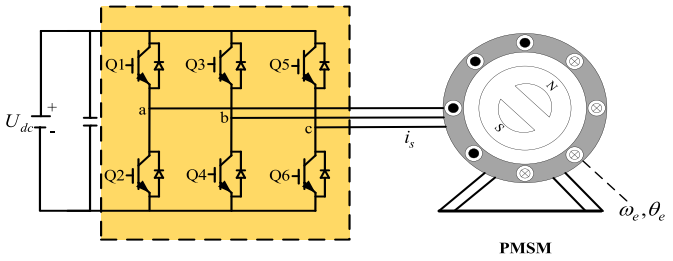

FIGURE 1. Two-level inverter drive PMSM topology.

In the two-level inverter, according to different switching sequences of the switches, 8 voltage vectors can be formed, and the distribution of each vector is shown in Fig. 2. $u_i\,(i = 1,2,3,4,5,6)$ are active voltage vectors, and u_0 and u_7 are zero vectors.

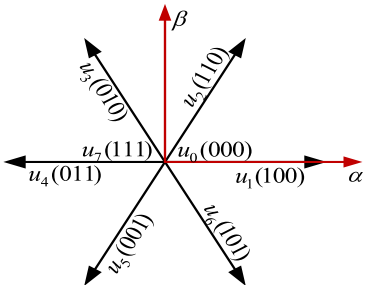

FIGURE 2. Voltage vector distribution.

2.2. PMSM Mathematical Model

The stator current equation of PMSM in the d-q coordinate system can be represented as follows:

$$\begin{cases} L_d \frac{di_d}{dt} = u_d - R_s i_d - e_d \\ L_q \frac{di_q}{dt} = u_q - R_s i_q - e_q \end{cases} \tag{1}$$

$$\begin{cases} e_d = -\omega_e L_q i_q \\ e_q = \omega_e \left(L_d i_d + \psi_f\right) \end{cases} \tag{2}$$

where R_s is the stator resistance. L_d and L_q are the stator inductances of the d-q axis. ψ_f is the permanent magnet flux linkage. ω_e is the electrical angular velocity. u_d, u_q, i_d, and i_q are the voltages and currents of the d-q axis, respectively. e_d and e_q are the d-q axis back EMF.

Using the first-order Eulerian discretization method typically utilized in engineering, the discretization of Eq. (1) is expressed as:

$$\begin{cases} i_d\left(k+1\right) = i_d\left(k\right) + \frac{T_s}{L_d}\left(u_d\left(k\right) - R_s i_d\left(k\right) - e_d\left(k\right)\right) \\ i_q\left(k+1\right) = i_q\left(k\right) + \frac{T_s}{L_q}\left(u_q\left(k\right) - R_s i_q\left(k\right) - e_q\left(k\right)\right) \end{cases} \tag{3}$$

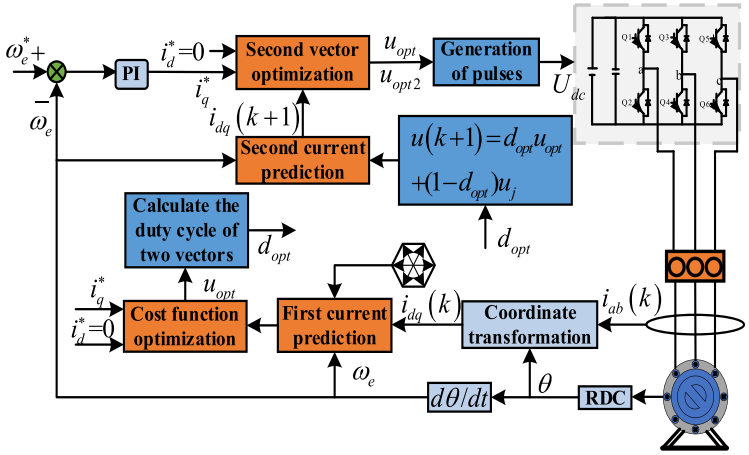

FIGURE 3. DV-MPCC strategy structure block diagram.

where $u_d(k)$ and $u_q(k)$ are the d-q axis voltage components at the constant k, respectively. $i_d(k+1)$ and $i_q(k+1)$ are the d-q axis current components at the constant $k+1$, respectively. $i_d(k)$ and $i_q(k)$ are the d-q axis current components at the constant k, respectively. $\omega_e(k)$ is the electrical angular velocity at the constant k. $e_d(k)$ and $e_q(k)$ are the d-q axis back EMF at the constant k, respectively. T_s is the sampling time.

3. DOUBLE VECTOR MODEL PREDICTIVE CURRENT CONTROL

To enhance the steady-state performance of conventional MPCC, a novel dual vector model predictive current controller (DV-MPCC) is proposed. Firstly, the first optimal active voltage vector is selected as the initial voltage vector by traversing the cost function. Secondly, to ensure the proximity of the reference voltage vector to the initial voltage vector, a voltage vector, either a zero vector or an effective vector that is close to the initial vector, is selected as the second standby voltage vector. Finally, the duty cycles of the two voltage vectors are allocated, the voltage combination that minimizes the cost function is selected for application to the inverter. The DV-MPCC strategy structure is shown in Fig. 3.

The initial voltage vector is selected by using Eq. (3) to predict the current for 6 active voltage vectors and then substituting them into Eq. (4) to select the active voltage vector that minimizes the cost function as the initial voltage vector.

$$g = |i_d^* - i_d(k+1)| + \left|i_q^* - i_q(k+1)\right| \tag{4}$$

where i_d^* and i_q^* are the d-q axis current reference components, respectively.

The d-q axis components of the synthesized voltage vector from two voltage vectors can be expressed as:

$$\begin{cases} u_d = u_{dopt} d_{opt} + (1 - d_{opt})\, u_{dj} \\ u_q = u_{qopt} d_{opt} + (1 - d_{opt})\, u_{qj} \end{cases} \tag{5}$$

where u_{dopt} and u_{qopt} are the voltage components of u_{opt} on the d-q axes d_{opt} is the duty cycle of u_{opt}, u_{dj} and u_{qj} are the voltage components of u_j on the d-q axes, and u_j is the two active voltage vectors or zero vector near the initial voltage vector.

By performing deadbeat control on the q-axis current, the duty cycle of the initial voltage vector can be derived:

$$d_{opt} = \frac{\Delta i_q + R_s i_q(k) + e_q(k) - u_{qj}}{u_{qopt} - u_{qj}} \tag{6}$$

where $\Delta i_q = L_q \frac{i_q^* - i_q(k)}{T_s}$.

DV-MPCC strategy implementation steps:

(1) By traversing the predicted current values of 6 effective voltage vectors through Eq. (3), the u_{opt} is determined to be the initial voltage vector to minimize the cost function in Eq. (4).

(2) By substituting the initial voltage vector duty cycle obtained from Eq. (6) into Eqs. (5) and (3), the corresponding predicted current for the selected combination can be obtained.

(3) The combination of u_{opt}, u_{opt2}, d_{opt}, and $1 - d_{opt}$, which minimizes the cost function, is selected and then applied to the inverter.

Based on the analysis, the distribution of the synthesized voltage vector in DV-MPCC is depicted by the red dashed line in Fig. 4. When the reference voltage vector u_s is between u_1 and u_2, it can be observed that the shortest path among Δu_1, Δu_2, and Δu_3 to u_1, u_2 and the boundary cannot meet the desired voltage error, which will cause the steady-state performance of the control system to deteriorate.

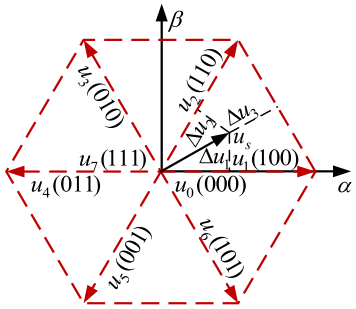

FIGURE 4. Synthesized voltage vector distribution of DV-MPCC.

4. DESIGN OF SDCM-MPCC STRATEGY

DV-MPCC strategy requires the use of cost function to traverse different voltage combinations, resulting in too much computa-

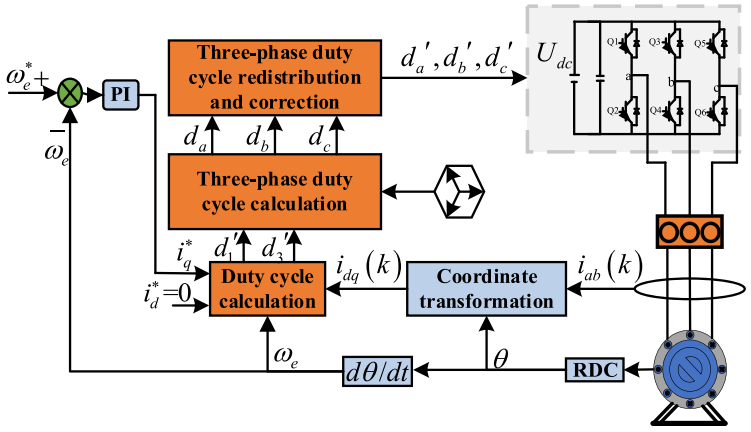

FIGURE 5. SDCM-MPCC structure block diagram.

tional burden. SDCM-MPCC strategy adopts the fixed voltage vectors u_1 and u_3 for control algorithm design and does not use cost function to traverse different voltage vector combinations. The three-phase duty cycle can be directly determined and directly applied to the two-level inverter without modulation. The simplified control algorithm offers a straightforward yet practical technical solution for the practical application of MPC in PMSM. The framework of the algorithm is presented in Fig. 5. SDCM-MPCC strategy consists of three parts: duty cycle calculation, three-phase duty cycle calculation, and three-phase duty cycle redistribution and correction. To illustrate that voltage vectors can be replaced equivalently, first analyze the selection and reconstruction of voltage vectors, and then elaborate on other components.

4.1. Selection and Reconstruction of Voltage Vector

SDCM-MPCC strategy focuses on three voltage vectors u_1, u_3, and u_5, which are called phase voltage vectors. The phase voltage vector satisfies $u_1+u_3+u_5=0$, and the duty cycle d_1, d_3, and d_5 of u_1, u_3, and u_5 correspond exactly to the three-phase duty cycle, that is, $d_1 \to d_a$, $d_3 \to d_b$, and $d_5 \to d_c$. When u_s is in sector I, it can be synthesized from u_1, u_3, and zero vector. The spatial distribution of the synthesized voltage vector is illustrated in Fig. 6. The three-phase voltage vectors are mutually independent and satisfy the superposition principle. Therefore, the reference voltage vector u_s can be vectorially composed by the three-phase voltage vectors in any hexagon region. Even if u_s is at the position of an active voltage vector u_2 at the vertex

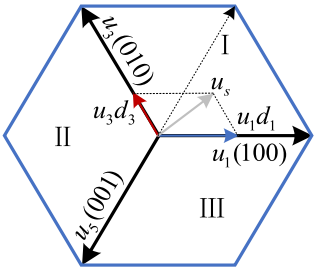

FIGURE 6. SDCM-MPCC synthetic voltage vector distribution.

of the regular hexagon, it can be obtained by u_1+u_3, and in this moment the duty cycles of both u_1 and u_3 are 1.

Since $u_1+u_3+u_5=0$, the control set can be further simplified. For clarity, Fig. 7 describes the decomposition and reconstruction of the voltage vector in the vector space.

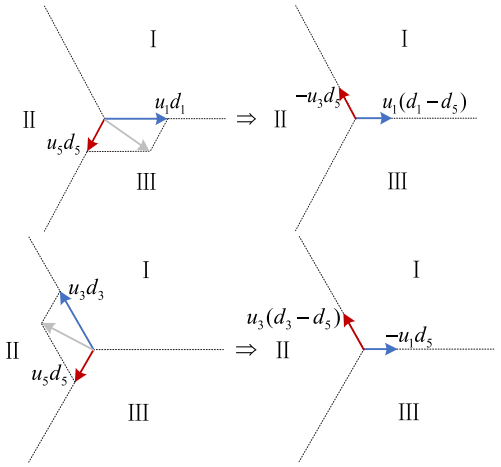

FIGURE 7. Decomposition and reconstruction of voltage vector.

When u_s is located in sector III, u_1 and u_5 are chosen as the active voltage vectors, and the duty cycles d_1 and d_5 are calculated by minimizing the current error. The lengths of the active voltage vectors can be represented by d_1u_1 and d_5u_5, respectively. In the meantime, if the fixed voltage vectors u_1 and u_3 are selected, the duty cycles of u_1 and u_3 are reconstructed into d_1-d_5 and $-d_5$, respectively, as shown in Eq. (7), and the synthesized voltage vectors have the same effect. If u_s is located in sector II, the duty cycle reconstruction formula for u_1 and u_3 is Eq. (8), with the same effect and consistent analysis principle, so it is not repeated here.

In summary, the voltage vector can be synthesized by u_1 and u_3 in any sector, so it is unnecessary to use the cost function to traverse different voltage combinations in the three sectors.

$$\begin{aligned} u_1d_1+u_5d_5 &= u_1d_1+(-u_1-u_3)\,d_5 \\ &= u_1\,(d_1-d_5)-u_3d_5 \\ u_3d_3+u_5d_5 &= u_3d_3+(-u_1-u_3)\,d_5 \end{aligned} \tag{7}$$

$$= u_3(d_3 - d_5) - u_1 d_5 \quad (8)$$

For convenience, the duty cycle of rewriting u_1 and u_3 is expressed as d_1' and d_3'. The combination of voltage vectors in different sectors can be expressed as:

$$\begin{aligned} u_1 d_1' + u_3 d_3' &= u_1 d_1' + u_3 d_3' && \text{I} \\ &= u_3(d_3' - d_1') - u_5 d_1' && \text{II} \\ &= u_1(d_1' - d_3') - u_5 d_3' && \text{III} \end{aligned} \quad (9)$$

4.2. Calculation of Duty Cycle

The components of u_1 and u_3 synthesized voltage vectors on the d-q axes are calculated as follows:

$$\begin{cases} u_d = u_{1d} d_1' + u_{3d} d_3' \\ u_q = u_{1q} d_1' + u_{3q} d_3' \end{cases} \quad (10)$$

According to Eqs. (3) and (10), deadbeat control is performed on the current of the d-q axes simultaneously, i.e., $i_d^* = i_d(k+1)$ and $i_q^* = i_q(k+1)$, then the duty cycle of u_1 and u_3 is expressed as:

$$\begin{cases} d_1' = \frac{(\Delta i_d + s_d)u_{3q} - (\Delta i_q + s_q)u_{3d}}{u_{1d}u_{3q} - u_{1q}u_{3d}} \\ d_3' = \frac{\Delta i_d + s_d - u_{1d}d_1'}{u_{3d}} \end{cases} \quad (11)$$

where $\begin{cases} \Delta i_d = L_d \frac{i_d^* - i_d(k)}{T_s} \\ s_d = R_s i_d(k) + e_d(k) \\ s_q = R_s i_q(k) + e_q(k) \end{cases}$.

4.3. Calculation of Three-Phase Duty Cycle

The three-phase duty cycle can be derived from d_1' and d_3'. When $d_1' > 0$ && $d_3' > 0$, this implies that the reference voltage vector resides in sector I, and the duty cycles d_a, d_b, and d_c of phases a, b, and c are $d_a = d_1'$, $d_b = d_3'$, and $d_c = 0$, respectively. The reason for $d_c = 0$ is that in sector I, only the upper and lower bridge switches of phases a and b are switched, while the switch of phase c remains off, similar to a five-segment wave generator.

When u_s falls within [0°, 60°] of sector I, the actual applied effective voltage vectors are u_1 and u_2. When u_s falls within [60°, 120°] of sector I, the actual applied effective voltage vectors are u_2 and u_3, and the zero vectors are all u_0. The corresponding vector diagram and three-phase duty cycle are shown in Fig. 8.

Based on Eq. (9), the three-phase duty cycle is calculated as follows:

(1) If $d_1' > 0$ && $d_3' > 0$, $d_a = d_1'$, $d_b = d_3'$, $d_c = 0$.

(2) If $d_1' < 0$ && $d_3' - d_1' > 0$, $d_a = 0$, $d_b = d_3' - d_1'$, $d_c = -d_1'$.

(3) If $d_3' < 0$ && $d_1' - d_3' > 0$, $d_a = d_1' - d_3'$, $d_b = 0$, $d_c = -d_3'$.

It should be noted that since only three sectors are divided, the three d_1', d_3', and $d_1' - d_3'$ judgments given have covered any situation. If other situations occur in d_1', d_3', and $d_1' - d_3'$, the three-phase duty cycle can be attributed to any sector, or else for (3).

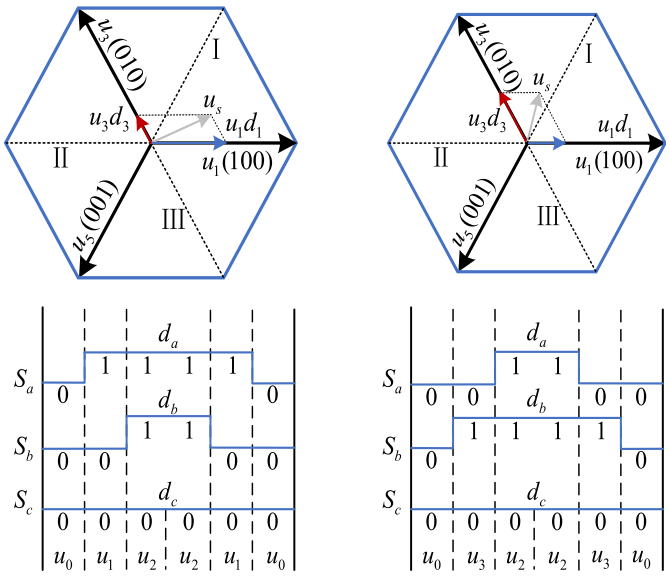

FIGURE 8. Voltage vector synthesized and three-phase duty cycle waveform of sector I.

4.4. Three-Phase Duty Cycle Redistribution and Correction

If the zero vector can be evenly distributed between u_0 and u_7, the steady-state performance can be further improved. The duty cycle of the zero vector is defined as follows:

$$d_0 = 1 - \max[d_a, d_b, d_c] \quad (12)$$

After obtaining zero vector duty cycle, the duty cycle of u_7 is expressed as follows:

$$d_{u_7} = (1 - \max[d_a, d_b, d_c])/2 \quad (13)$$

At this time, the three-phase duty cycle is redistributed as shown in Eq. (14). The three-phase duty cycle in Fig. 8 is updated as shown in Fig. 9.

$$\begin{cases} d_a' = d_a + (1 - \max[d_a, d_b, d_c])/2 \\ d_b' = d_b + (1 - \max[d_a, d_b, d_c])/2 \\ d_c' = d_c + (1 - \max[d_a, d_b, d_c])/2 \end{cases} \quad (14)$$

When the speed or load suddenly changes, the three-phase duty cycles d_a', d_b', and d_c' may exceed the range of [0, 1], requiring further correction. Possible situations include the following:

(1) If the duty cycle is less than 0, it is set to 0.

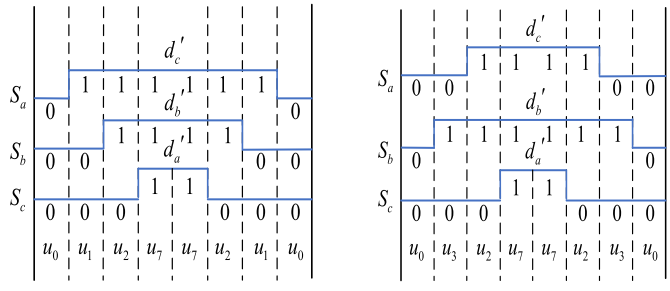

FIGURE 9. Three-phase duty cycle waveform of sector I after zero vector average distribution.

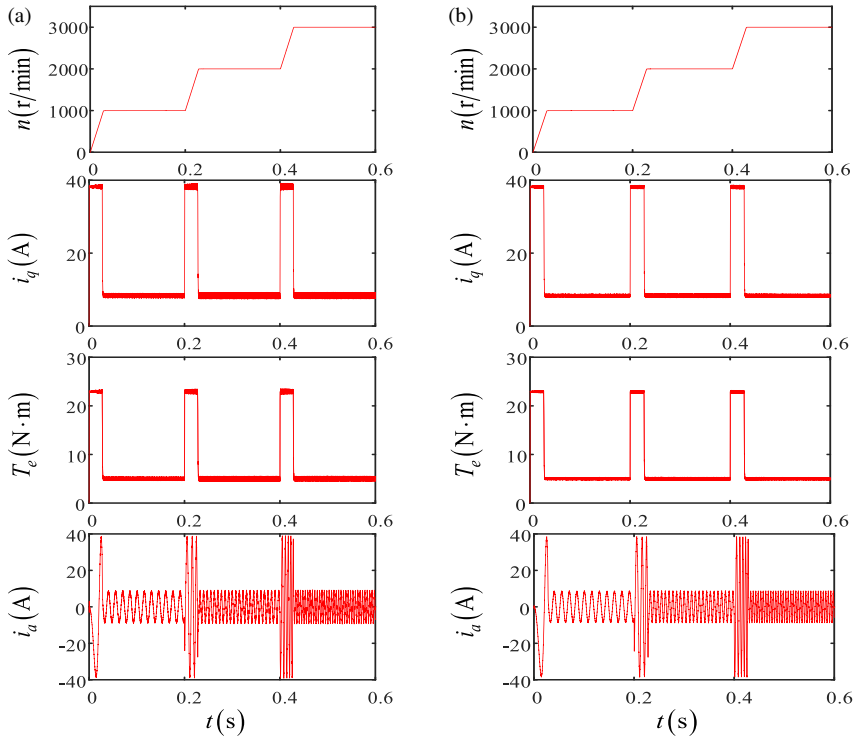

FIGURE 10. Speed, current, and torque waveforms of the two strategies at variable speed with load torque of 5 N·m. (a) DV-MPCC. (b) SDCM-MPCC.

(2) If the duty cycle exceeds 1, reconstruction is required to maintain the ratio of the three-phase duty cycles unchanged.

Taking $d'_a > 1$ as an example, the reassignment is as follows:

$$\begin{cases} d'_a = 1 \\ d'_b = d'_b/d'_a \\ d'_c = d'_c/d'_a \end{cases} \tag{15}$$

The steps to implement the SDCM-MPCC strategy are outlined below:

(1) Calculate the duty cycle of u_1 and u_3 through Eq. (11).

(2) The positive and negative values of d'_1, d'_3, and $d'_1 - d'_3$ are used to determine the sector, and then the three-phase duty cycle is determined.

(3) Through Eq. (13), the duty cycle of u_7 is obtained. Further, the three-phase duty cycle is redistributed according to Eq. (14), and the final three-phase duty cycle is corrected according to the proposed strategy.

5. SIMULATION ANALYSIS

The DV-MPCC and SDCM-MPCC strategies on the same motor are compared and analyzed by Matlab/Simulink. The motor parameters are shown in Table 1. As a surface-mounted PMSM is used, the control mode with $i_d^* = 0$ is adopted. Both control strategies maintain a sampling frequency of 10 kHz and the same proportional-integral (PI) parameters ($k_p = 2.7$, $k_i = 40$).

TABLE 1. The PMSM parameters.

Parameter	Value	Unit
Number of pole pairs	4	
Stator resistance	0.15	Ω
Stator inductance	1.625	mH
Permanent magnet flux	0.1	Wb
Moment of inertia	4.78	g·cm^2
Rated power	4.5	kW
Rated speed	3000	r/min
Rated torque	15	N·m
Rated voltage	300	V
Peak current	38.8	A

5.1. Comparison of Dynamic Performance

(1) Operating conditions: reference speed 1000 r/min, load torque 5 N·m, sudden change of speed to 2000 r/min at 0.2 s, sudden change of speed to 3000 r/min at 0.4 s.

Under constant load torque and variable speed operation conditions, the speed, current, and torque waveforms for the two control strategies are presented in Fig. 10. Both control strategies reach 1000 r/min at 0.029 s, accelerate to 2000 r/min at 0.229 s, and accelerate to the rated value at 0.429 s, with almost no overshoot and steady-state error in speed. With the same PI parameters, the speed dynamic performances of both strategies are essentially the same. The current and torque of both strategies can well follow the changes in speed and load without overshoot. Since $i_d^* = 0$ control is adopted, the amplitude variations in i_q, T_e, and i_a are consistent with the theory.

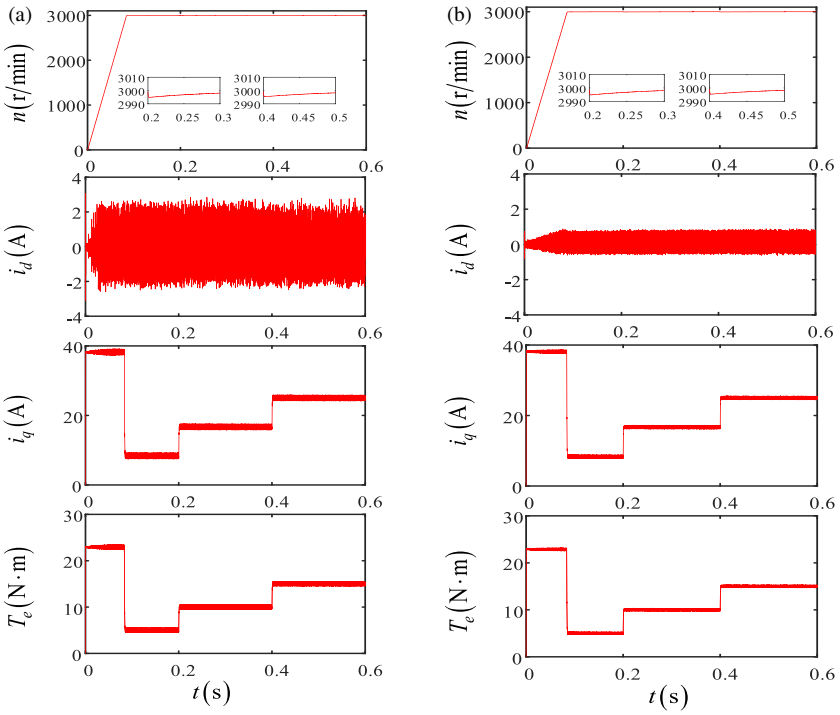

FIGURE 11. Speed, current, and torque waveforms of the two control strategies at rated speed and different load torques. (a) DV-MPCC. (b) SDCM-MPCC.

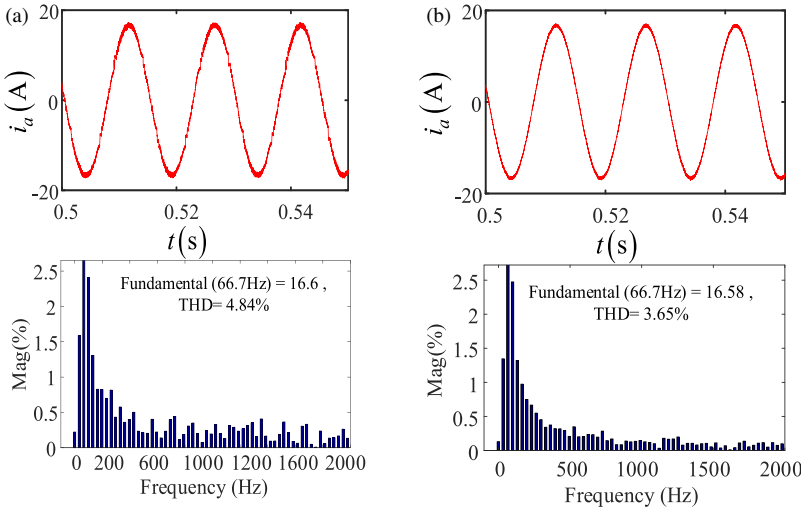

FIGURE 12. i_a and FFT harmonic analysis of two strategies at 1000 r/min and 10 N·m. (a) DV-MPCC. (b) SDCM-MPCC.

(2) Operating conditions: reference speed 3000 r/min, load torque 5 N·m, sudden change to 10 N·m at 0.2 s, sudden change to 15 N·m at 0.4 s.

Figure 11 shows the speed, current, and torque waveforms for two strategies operating under constant speed and varying load torque conditions. Both strategies reach rated speed at 0.068 s after motor start-up, and the speed recovers to 3000 r/min at 0.28 s and 0.47 s after a sudden increase in load torque at 0.2 s and 0.4 s, respectively, with the speed dropping by 5 r/min in both cases. Because DV-MPCC strategy only uses deadbeat control for i_q, it is observed that the i_d ripple is relatively large.

5.2. Comparison of Steady-State Performance

(1) Operating conditions: speed 1000 r/min, load torque 10 N·m.

The steady-state phase current and its ' analysis for the two strategies at a reference speed of 1000 r/min and load torque of 10 N·m are illustrated in Fig. 12. The figure demonstrates the figure that the stator current waveform of SDCM-MPCC is better than that of DV-MPCC. The THD of the DV-MPCC strategy is 4.84%, while the THD of the SDCM-MPCC strategy is 3.65%. The results indicate that the proposed strategy reduces phase current harmonics and improves steady-state performance.

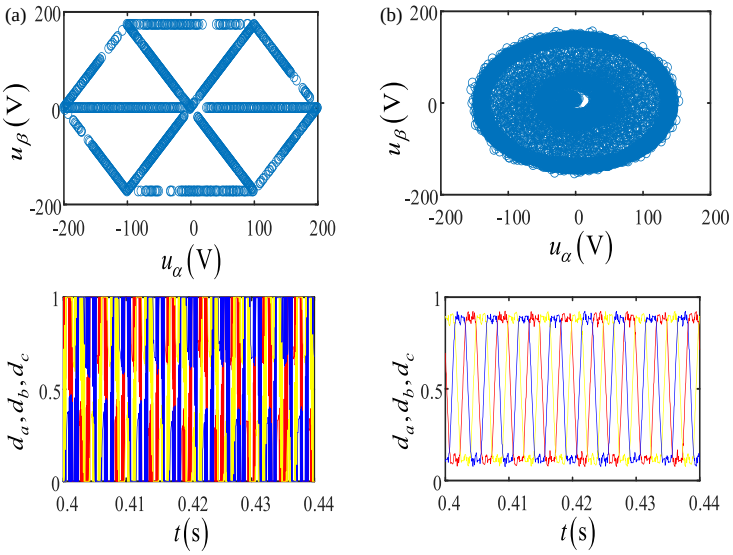

FIGURE 13. Output voltage and three-phase duty cycle waveform. (a) DV-MPCC. (b) SDCM-MPCC.

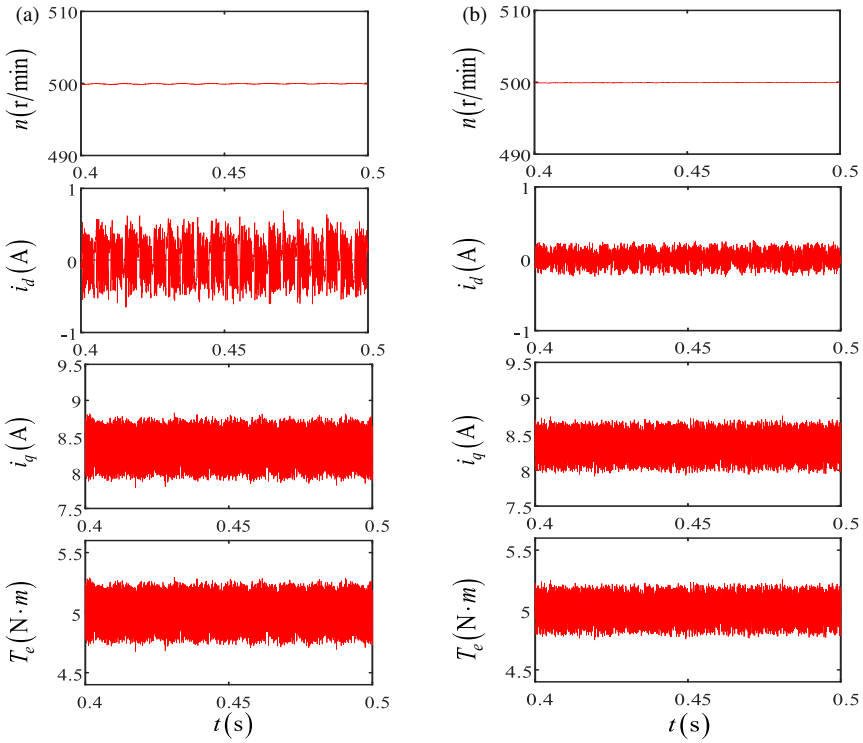

FIGURE 14. Speed, current, and torque waveforms of two strategies at 500 r/min and 5 N·m. (a) DV-MPCC. (b) SDCM-MPCC.

(2) Operating conditions: speed 3000 r/min, load torque 15 N·m.

Figure 13 displays the waveforms of output voltage and a section of three-phase duty cycle. DV-MPCC uses only two voltage vectors, resulting in discontinuous output voltage and abrupt changes in three-phase duty cycle. When the output voltage vector is at a regular hexagon boundary, it is a combination of active voltage vectors. When the output voltage is on the active voltage vector axis, it is the combination of the active voltage vector and the zero vector, which is consistent with theoretical analysis. While the SDCM-MPCC strategy uses three voltage vectors, and the output voltage vectors are continuously distributed. Due to its three-phase duty cycle being adjusted according to Eq. (14), the duty cycle of the saddle wave is output. The results evidence that the SDCM-MPCC strategy reduces current ripple, suppresses phase current harmonics, and improves waveform quality.

(3) Operating conditions: speed 500 r/min, load torque 5 N·m.

Figure 14 displays the speed, current, and torque waveforms of the two strategies at low-speed and light-load at steady state.

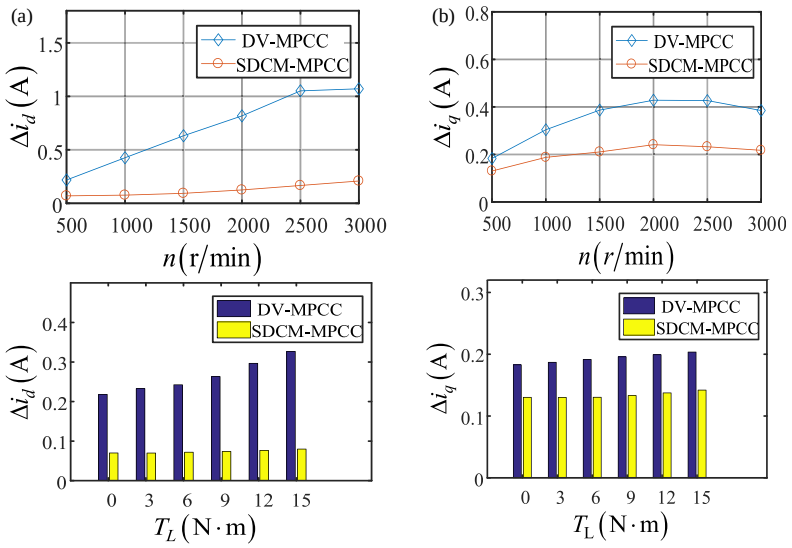

FIGURE 15. The ripple of d-q axis current for two strategies at no load, different speeds and 500 r/min, different load torques.

The results indicate that both strategies basically no static error in speed. For DV-MPCC strategy, the fluctuation ranges of i_d, i_q, and T_e are [−0.6 A, 0.6 A], [7.9 A, 8.8 A], and [4.74 N·m, 5.28 N·m], respectively, while for the SDM-MPCC strategy, the fluctuation ranges of i_d, i_q, and T_e are [−0.22 A, 0.22 A], [8 A, 8.7 A], and [4.8 N·m, 5.22 N·m], respectively. This indicates that the SDCM-MPCC strategy has smaller ripple in the current and torque of the d-q axis and better steady-state performance.

(4) Operating conditions: no-load speed of 500 r/min, 1000 r/min, 1500 r/min, 2000 r/min, 2500 r/min, 3000 r/min, and 500 r/min, load torques of 0 N·m, 3 N·m, 6 N·m, 9 N·m, 12 N·m, 15 N·m.

Figure 15 shows the current ripple line chart for DV-MPCC and SDCM-MPCC strategies at no-load speeds of 500 r/min, 1000 r/min, 1500 r/min, 2000 r/min, 2500 r/min, and 3000 r/min, and the current ripple rectangular chart for both control strategies at 500 r/min and load torques of 0 N·m, 3 N·m, 6 N·m, 9 N·m, 12 N·m, and 15 N·m. A total of 6,000,001 sets of data are extracted, and the current ripple is calculated by Eq. (16). The results show that the current ripple of SDCM-MPCC strategy is smaller than that of DV-MPCC strategy in the whole speed range.

At 500 r/min no load, the Δi_d of DV-MPCC and SDCM-MPCC strategies are 0.2181 A and 0.07 A, and Δi_q are 0.1830 A and 0.1303 A, respectively. Δi_d of SDM-MPCC strategy decreased by 0.1481 A and Δi_q by 0.0527 A compared to DV-MPCC strategy. Δi_d of SDM-MPCC strategy decreases by 72.07% and Δi_q by 29.5% on average compared to the DV-MPCC strategy for different load torques.

$$\begin{cases} \Delta i_d = \sqrt{\dfrac{1}{N}\displaystyle\sum_{n=1}^{N}\left(i_d\left(n\right) - i_{d\text{-}ave}\right)^2} \\ \Delta i_q = \sqrt{\dfrac{1}{N}\displaystyle\sum_{n=1}^{N}\left(i_q\left(n\right) - i_{q\text{-}ave}\right)^2} \end{cases} \tag{16}$$

where N is the number of samples, $-i_{d\text{-}ave}$ and $i_{q\text{-}ave}$ are the average values of i_d and i_q, $i_d(n)$ and $i_q(n)$ are the d-q axis currents at the moment n.

5.3. Comparison of Algorithm Execution Time

The core algorithms of DV-MPCC and SDCM-MPCC strategies are tested 10^5 times repeatedly using the 'tic' and 'toc' functions in MATLAB. The average of prediction times and execution time for both strategies are shown in Table 2. DV-MPCC strategy requires 9 prediction times with an algorithm execution time of 0.5590 s, while SDCM-MPCC strategy does not require iterations and only generates the drive signal by online calculation with an execution time of 0.4561 s. Compared with DV-MPCC strategy, the execution time of the proposed strategy is shortened by 18.4%, indicating that the algorithm is more efficient.

TABLE 2. The core algorithm execution time and prediction times of two control strategies.

strategy	DV-MPCC	SDCM-MPCC
prediction times	9	1
execution time	0.5590 s	0.4561 s

6. EXPERIMENTAL VERIFICATION

To validate the effectiveness of the method proposed, the RT LAB (OP5600) platform used is shown in Fig. 16, and its hardware in the loop system (HILS) configuration diagram is shown in Fig. 17. The DSP adopts TMS320F2812, and the inverter and PMSM are created by RT-LAB. The experimental conditions such as motor and PI parameters are consistent with the simulation.

The speed, current and torque waveforms of the two strategies under constant load torque and variable speed conditions are shown in Fig. 18. The graph shows both strategies reach

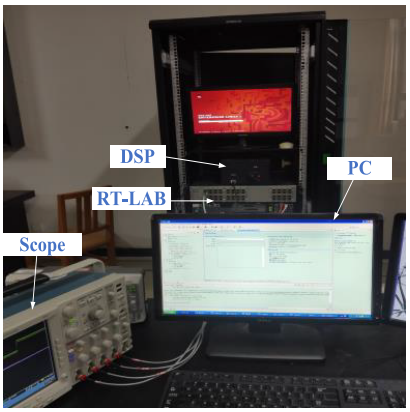

FIGURE 16. RT-LAB experiment platform.

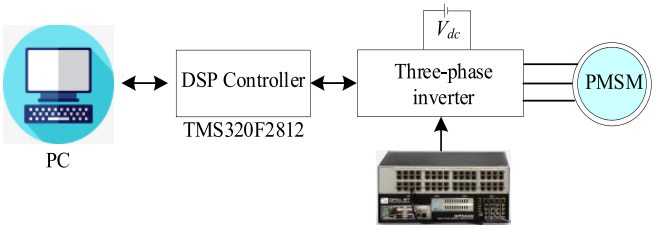

FIGURE 17. RT-LAB hardware-in-the-loop system configuration.

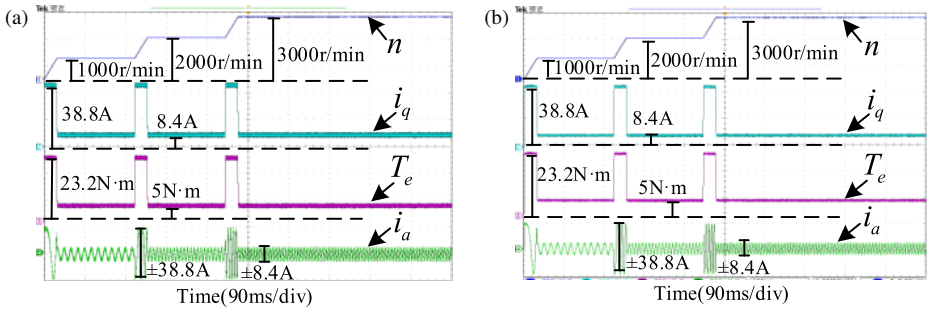

FIGURE 18. Constant load torque, speed, current and torque experimental waveforms at variable speed. (a) DV-MPCC. (b) SDCM-MPCC.

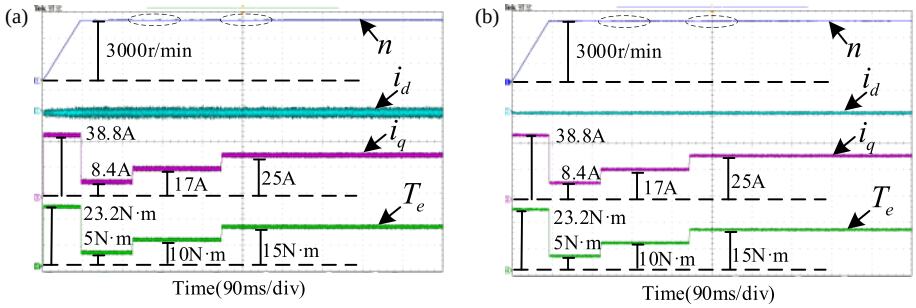

FIGURE 19. Speed, current and torque experimental waveforms with constant speed and variable load torque. (a) DV-MPCC. (b) SDCM-MPCC.

1000 r/min at 0.030 s. The reference speed is 2000 r/min at 0.2 s, and accelerate to 2000 r/min at 0.231 s. The reference speed is 3000 r/min at 0.4 s, and accelerate to the rated speed at 0.432 s, with basically no overshoot and static error in speed. The current and torque can follow the speed and load torque changes well, and there is basically no overshoot and static error. The experimental results demonstrate that the dynamic performance of the two strategies is basically identical.

Figure 19 shows the speed, current, and torque waveforms of the two strategies with constant speed and variable load torque. From Fig. 19, both strategies reach the motor starting speed of 3000 r/min at 0.086 s, and the speed returns to 3000 r/min at 0.29 s after a sudden increase of 10 N·m load torque at 0.2 s. Similarly, the speed returns to 3000 r/min at 0.49 s after a sudden increase of 15 N·m load torque at 0.4 s, and the speed drops by 8 r/min in both cases. The results demonstrate that the dynamic performance of the both strategies in terms of speed, current, and torque are basically consistent.

Under the condition of 1000 r/min and 10 N·m, the phase current and fast Fourier transform (FFT) analysis of the two strategies are presented in Fig. 20. From Fig. 20, the harmonics of the phase current in SDCM-MPCC strategy are smaller than those in DV-MPCC strategy. The total harmonic distortion (THD) of the two strategies is 7.83% and 4.17%, respectively, indicating that SDCM-MPCC strategy has better effect on suppressing phase current harmonics.

Figure 21 shows the steady-state waveforms at 500 r/min and 5 N·m load torque. From Fig. 21, the steady-state performance of SDCM-MPCC strategy has been improved to a certain extent. To effectively demonstrate that SDCM-MPCC

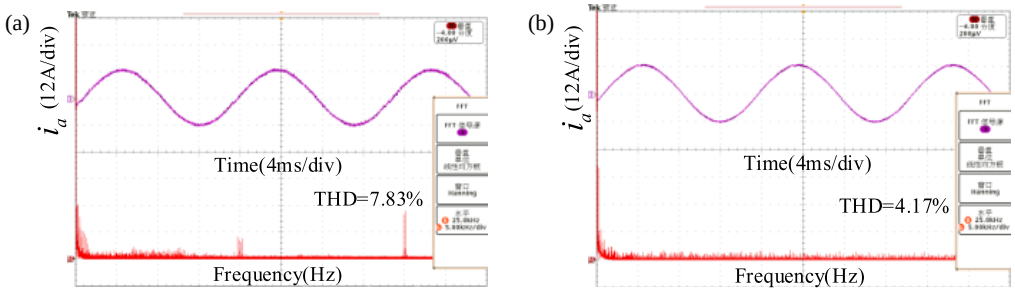

FIGURE 20. Steady-state phase current experimental waveform and FFT analysis. (a) DV-MPCC. (b) SDCM-MPCC.

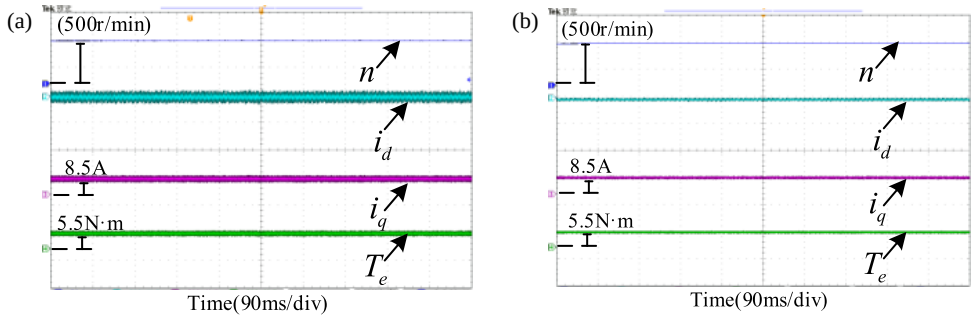

FIGURE 21. Speed, current, and torque experimental waveforms at steady state. (a) DV-MPCC. (b) SDCM-MPCC.

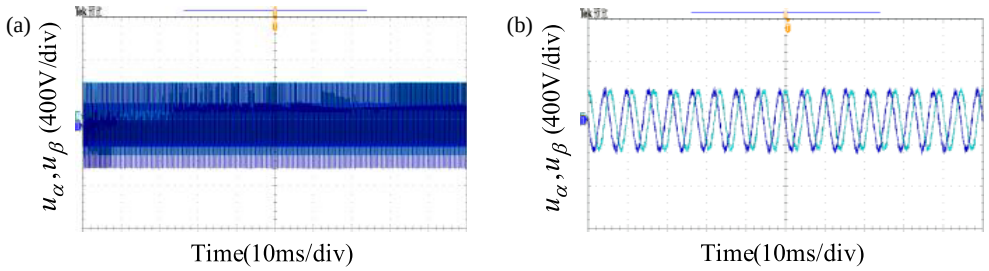

FIGURE 22. Output voltage experimental waveforms. (a) DV-MPCC. (b) SDCM-MPCC.

TABLE 3. Current ripple at 500 r/min and 5 N·m.

Strategies	Operating conditions	Δi_d/A	Δi_q/A
DV-MPCC	500 r/min, 5 N·m	0.5561	0.2611
SDCM-MPCC		0.1278	0.1332

strategy improves steady-state performance, the current ripple of the two strategies are calculated using Eq. (16), and the results are shown in Table 3. The data shows that the Δi_d and Δi_q of SDCM-MPCC strategy are decreased by 0.4283 A and 0.1279 A, respectively, indicating that SDCM-MPCC strategy exhibits superior steady-state performance.

Figure 22 displays the output voltage waveforms of both strategies at 3000 r/min and 15 N·m. As can be seen from the figure, the u_α and u_β components of SDCM-MPCC strategy are standard sine waves. According to Euler's formula, the synthesized voltage is circular, indicating that its output voltage is continuously distributed and can cover any amplitude and direction. However, DV-MPCC strategy uses two non-fixed voltage vectors, resulting in discontinuous output voltage and frequent switching. Therefore, the output voltage vector range of the SDCM-MPCC strategy is wider, which can effectively suppress current ripple and harmonics caused by voltage errors.

Figure 23 shows the three-phase duty cycle waveforms for both strategies under 3000 r/min and 15 N·m. As shown in the figure, the duty cycle of the DV-MPCC strategy output voltage is not continuously distributed, but always jumps between 0 and 1. However, the duty cycle of the SDCM-MPCC strategy output voltage is a saddle wave. The results demonstrate that SDCM-MPCC strategy can improve steady-state performance.

To compare their computational complexity, the execution times for both algorithms are presented in Fig. 24. From Fig. 24, SDCM-MPCC algorithm simplifies the process of duty cycle calculation and cost function optimization, and the execution time of this algorithm is 26 µs. However, the execution time of DV-MPCC strategy is 45 µs. The experimental results show that SDCM-MPCC strategy reduces the execution time.

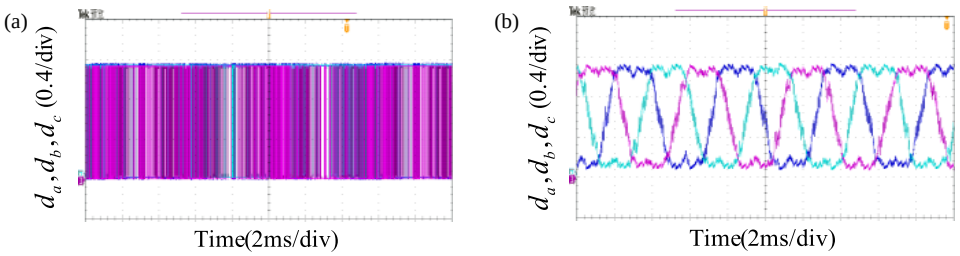

FIGURE 23. Three-phase duty cycle experimental waveforms. (a) DV-MPCC. (b) SDCM-MPCC.

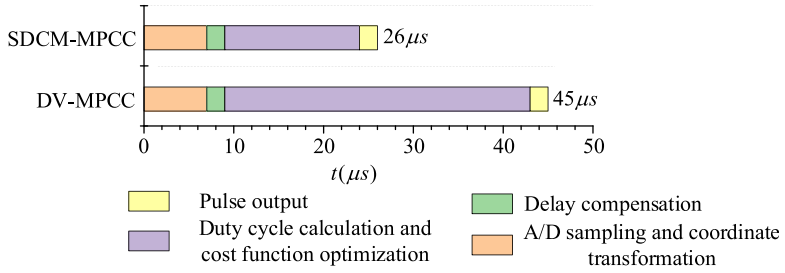

FIGURE 24. The execution time of the two strategies.

7. CONCLUSION

To reduce the prediction times and algorithm complexity of MPCC and get good steady-state performance, a novel SDCM-MPCC strategy is proposed. Through simulation and experimental verification, the following conclusions are obtained:

(1) The dynamic performances of the two strategies are basically consistent. However, compared to DV-MPCC strategy, SDCM-MPCC strategy can simultaneously achieve deadbeat control for both *d*-*q* axis currents, reduce phase current harmonics by 46.74%, and have smaller current ripples, improved steady-state performance.

(2) SDCM-MPCC strategy uses two fixed voltage vectors, and the duty cycles of the three phases can be directly determined, without using cost functions to traverse voltage vector combinations. Compared with DV-MPCC strategy, its execution time is accelerated by 19 μs, and its complexity is lower.

ACKNOWLEDGEMENT

This work was supported by the Scientific Research Fund of Hunan Provincial Education Department under Grant Number 23B1017.

REFERENCES

[1] Shao, Z., Z. Ma, J. Gong, and Y. Peng, "Torque ripple suppression synchronous optimal PWM for IPMSMs by reallocating current harmonics in multiple synchronous reference frame," *IEEE Transactions on Power Electronics*, 2025.

[2] Azom, M. A. and M. Y. A. Khan, "Recent developments in control and simulation of permanent magnet synchronous motor systems," *Control Systems and Optimization Letters*, Vol. 3, No. 1, 84–91, 2025.

[3] Li, F., X. Qiu, H. Wang, W. Zhang, and Z. Zhang, "Dynamic performance optimization of deadbeat predictive current control for PMSM by gain self-tuning technology," *IEEE Journal of Emerging and Selected Topics in Power Electronics*, Vol. 13, No. 2, 1856–1865, 2024.

[4] König, P., D. Sharma, K. R. Konda, T. Xie, and K. Höschler, "Comprehensive review on cooling of permanent magnet synchronous motors and their qualitative assessment for aerospace applications," *Energies*, Vol. 16, No. 22, 7524, 2023.

[5] Zhang, X. and S. Fang, "A simple model predictive current control for PMSM drives based on harmonic current extraction," *IEEE Transactions on Industrial Electronics*, Vol. 72, No. 4, 3324–3334, 2025.

[6] Wang, H., C. Gan, C. Zhang, H. Ren, and R. Qu, "Parameter robust predictive current control for PMSM drives based on self-tuning incremental model and voltage constraint compensation," *IEEE Transactions on Power Electronics*, 2025.

[7] Huang, K., X. Lin, T. Wu, T. Luo, W. Wang, T. Liu, and D. Zhang, "An extended model predictive control for PMSM with minimum ripples and small runtimes," *IEEE Transactions on Industrial Electronics*, 2025.

[8] Xu, Y., B. Zhang, and Q. Zhou, "Two-vector based model predictive current control for permanent magnet synchronous motor," *Transactions of China Electrotechnical Society*, Vol. 32, No. 20, 222–230, 2017.

[9] Lin, H. and W. Song, "Three-vector model predictive current control of permanent magnet synchronous motor based on SVM," in *2019 IEEE International Symposium on Predictive Control of Electrical Drives and Power Electronics (PRECEDE)*, 1–6, Quanzhou, China, 2019.

[10] Xu, B., Q. Jiang, W. Ji, and S. Ding, "An improved three-vector-based model predictive current control method for surface-mounted PMSM drives," *IEEE Transactions on Transportation Electrification*, Vol. 8, No. 4, 4418–4430, 2022.

[11] Wu, X., Y. Wang, N. Wang, H. Xing, W. Xie, and C. H. T. Lee, "A novel double-vector model predictive current control for PMSM with low computational burden and switching frequency," *IEEE Transactions on Power Electronics*, 2025.

[12] Wang, C., J. Ji, H. Tang, T. Tao, and W. Zhao, "Improved model predictive current control for linear vernier permanent-magnet motor with efficient voltage vectors selection," *IEEE Transactions on Industrial Electronics*, Vol. 70, No. 3, 2833–2842, Mar. 2023.

[13] Shadmand, M. B., S. Jain, and R. S. Balog, "Autotuning technique for the cost function weight factors in model predictive control for power electronic interfaces," *IEEE Journal of Emerging and Selected Topics in Power Electronics*, Vol. 7, No. 2, 1408–1420, 2018.

[14] Wen, D., W. Zhang, Z. Tang, X. Zhang, and Z. Cheng, "Model predictive control with ESO and an improved speed loop for PMSM," *Progress In Electromagnetics Research C*, Vol. 142, 107–117, 2024.

[15] Sangsefidi, Y., S. Ziaeinejad, and A. Mehrizi-Sani, "Low switching frequency-based predictive control of a grid-connected voltage-sourced converter," *IEEE Transactions on Energy Conversion*, Vol. 32, No. 2, 686–697, 2016.

[16] Wang, Y., Y. Zhang, H. Yang, and J. Rodriguez, "Variable-vector-based model predictive control with reduced current harmonic and controllable switching frequency for PMSM drives," *IEEE Transactions on Power Electronics*, Vol. 39, No. 12, 16 429–16 441, 2024.

[17] Zhang, H., S. Zhu, J. Jiang, Q. Wang, A. Wang, and D. Jin, "Simplified model prediction current control strategy for permanent magnet synchronous motor," *Journal of Power Electronics*, Vol. 22, No. 11, 1860–1871, 2022.

[18] Wu, X., Y. Zhang, F. Shen, M. Yang, T. Wu, S. Huang, and H. Cui, "Equivalent three-vector-based model predictive control with duty-cycle reconstruction for PMSM," *IEEE Transactions on Industrial Electronics*, Vol. 71, No. 3, 2395–2404, 2023.

[19] Cui, J., T. Tao, and W. Zhao, "Optimized control set model predictive control for dual three-phase PMSM with minimum error duty cycle regulation," *IEEE Transactions on Power Electronics*, Vol. 39, No. 1, 1319–1332, 2023.

[20] Parvathy, M. L., K. Eshwar, and V. K. Thippiripati, "A modified duty-modulated predictive current control for permanent magnet synchronous motor drive," *IET Electric Power Applications*, Vol. 15, No. 1, 25–38, 2021.

[21] Petkar, S. G. and V. K. Thippiripati, "Enhanced predictive current control of PMSM drive with virtual voltage space vectors," *IEEE Journal of Emerging and Selected Topics in Industrial Electronics*, Vol. 3, No. 3, 834–844, 2021.

[22] Sun, J., Y. Yang, R. Chen, X. Zhang, C. S. Lim, and J. Rodriguez, "An efficient multi-vector-based model predictive current control for PMSM drive," *CPSS Transactions on Power Electronics and Applications*, Vol. 9, No. 1, 79–89, 2023.